

Ultra-smooth silicon nitride waveguides based on the Damascene reflow process: fabrication and loss origins: supplementary material

MARTIN H. P. PFEIFFER¹, JUNQIU LIU¹, ARSLAN S. RAJA¹, TIAGO MORAIS¹,
BAHAREH GHADIANI¹, AND TOBIAS J. KIPPENBERG^{1,*}

École Polytechnique Fédérale de Lausanne (EPFL), Laboratory of Photonics and Quantum Measurements (LPQM), Lausanne, CH-1015, Switzerland

*Corresponding author: tobias.kippenberg@epfl.ch

Published 20 July 2018

This document provides supplementary information to "Ultra-smooth silicon nitride waveguides based on the Damascene reflow process: fabrication and loss origins," <https://doi.org/10.1364/optica.5.000884>.

1. WAFER PROCESSING OVERVIEW

Table S1 lists the processing details of the individual wafers fabricated for this loss study as well as their final heights. Due to the imprecision of chemical mechanical planarization and etching processes the height and width dimensions statements have margins of ± 30 nm and ± 50 nm respectively.

2. THERMAL BISTABILITY SETUP AND METHOD

In the following details concerning the measurement setup, parameter estimation and fitting methods for the thermal bistability spectroscopy are described. The setup allows for automatic acquisition of the resonance drag for a single resonance and is schematically shown in Figure S1a). An ECDL (Toptica CTL) provides up to 40 mW of optical power within the spectral range from 1460 nm to 1570 nm. Two optical switches allow to measure the resonance drag from both directions without reconnecting any fiber. The incident power on the chip as well as a frequency calibrated resonance lineshape measurement are recorded. Based on a calibration of the detector response and the setup transmission using power meters, the detector voltage can be converted into power at the chip output. Polarization maintaining fiber is used throughout the setup to ensure a stable incident polarization. Based on the assumption that the thermal resonance drag needs to be equal for both measurement directions the measured power levels before and after the chip can be used to calculate the individual coupling losses per facet.

Measurement of thermal resonance shift The resonance shift upon heating described by $\beta(\omega)$ can be measured easily using a temperature-controlled sample stage and values of 2.5 GHz/K and 2.63 GHz/K have been reported earlier [1, 2]. We measure

the resonance shift upon constant heating for samples with and without SiO₂ top-cladding. To this end, an ECDL is scanned continuously across the resonance while the set point of the sample stage's temperature controller is step-wise changed. Accurate frequency calibration is achieved as before through referencing the ECDL scan to a frequency comb and a Mach-Zehnder interferometer. Hereby the frequency comb signal is used to locally calibrate the FSR of the continuous interferometric signal. As a nonlinear broadened frequency comb signal is used this technique alleviates tedious adjustments of the comb marker calibration signal. Additionally, the beat signal with a stable reference laser is used to provide an absolute calibration signal. We perform measurements for resonances of the fundamental quasi-TE modes of the cladded and non-cladded samples at three wavelengths. The results are shown in Figure S1b) and are in excellent agreement with previously published values. Through a linear fit of the measured values $\beta(\omega)$ is determined.

Simulation of thermal resistance The thermal resistance can be simulated using a finite-element model implementing the heat transport equations for the steady-state in two dimensions. As model geometry a $1.5 \times 0.8 \mu\text{m}^2$ waveguide is used here and consists of three materials (Si, SiO₂, Si₃N₄) whose thermal properties are taken as:

The bulk Si substrate is assumed as a heat bath being constantly at room temperature. Similarly, we assume constant room temperature as boundary condition for the lateral borders which are placed with 10 μm distance from the waveguide core. This justifies the lateral boundary conditions as the heat transport is dominated by the cooling of the bulk Si substrate and the sample top surface. Accurate modelling of the radiative and convective cooling effects on the sample top surface

wafer	1	2	3	4	5	6
Waveguide pattern lithography	E-beam lithography			Stepper lithography		
Filler pattern lithography	Photolithography			Stepper lithography		
Preform etch mask	amorphous Si hardmask			DUV photoresist with BARC		
Preform etch	dry etch based on He and C ₄ F ₈					
Preform reflow	-	anneal at 1250°C in N ₂ atmosphere for 18h				
Si ₃ N ₄ deposition	LPCVD process at 775°C and 200 mT based on SiCl ₂ H ₂ (30 sccm) and NH ₃ (180 sccm)					
Planarization	Fumed SiO ₂ particle slurry based CMP					
Si ₃ N ₄ anneal	1200°C in N ₂ for 24h	1200°C in N ₂ for 11h	1200°C in N ₂ for 3h			
Cladding deposition	3 μm low temperature oxide (425°C, SiH ₄ + O ₂)				-	-
Cladding anneal	anneal at 1200°C in N ₂ atmosphere for 3h				-	-
waveguide height	850 nm	650 nm	615 nm	620 nm	750 nm	700 nm

Table S1. Summary of process parameters for the individual wafers analyzed for this study.

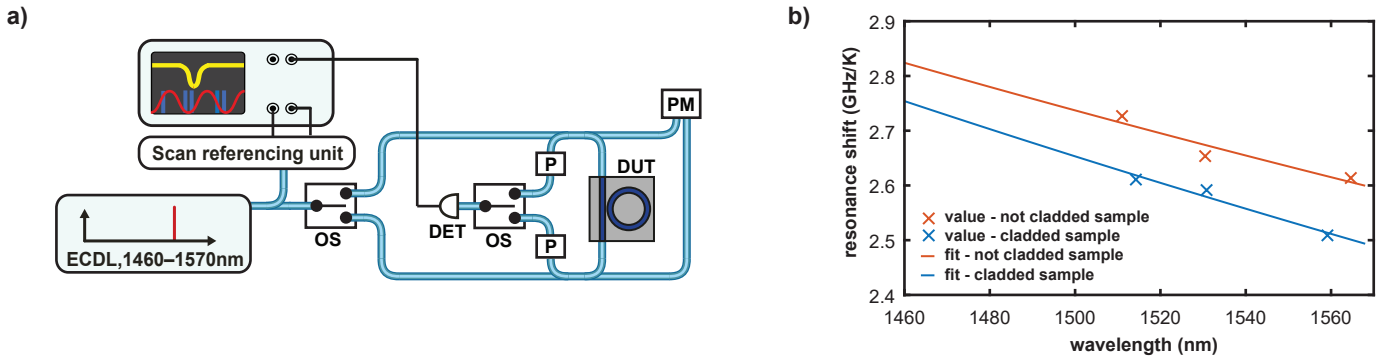


Fig. S1. a) Setup used to record resonance skewing upon driving laser power increase. OS: optical switch, DET: photodetector, PM: power meter, DUT: device under test, P: polarizer. b) Resonance shift upon constant heating characterized for cladded and non-cladded samples, as well as fit with a linear function.

material	heat capacity	density	thermal conductivity
SiO ₂	1000 J/(kgK)	2200 kg/m ³	1.38 W/(mK)
Si ₃ N ₄	700 J/(kgK)	3100 kg/m ³	20 W/(mK)
Si	700 J/(kgK)	2329 kg/m ³	130 W/(mK)

are difficult to implement. This is why we estimate limiting values by assuming either a boundary at room temperature or perfect thermal isolation. Moreover, we test in the case of the fully cladded device whether the absorption location plays an important role assuming thermal isolation at the top surface. Negligible difference is observed for the cases of heating inside the waveguide core, in a 100 nm thick boundary layer extending to equal amounts into the core and the cladding or within a 300 nm thick layer in the top cladding with the same width of the waveguide.

Using the difference of waveguide core average temperature to the boundary condition's room temperature, the local temperature difference ΔT is computed. For a heating power P_{heating} the thermal resistance follows as $R_{\text{th}} = \Delta T / P_{\text{heating}}$. For the cladded geometry we find values of $R_{\text{th}} = 216 \text{ K/W}$ and $R_{\text{th}} = 157 \text{ K/W}$ as limits for thermal insulation and perfect

cooling respectively. For the non-cladded geometry we find $R_{\text{th}} = 286 \text{ K/W}$ and $R_{\text{th}} = 6 \text{ K/W}$ as limits for thermal insulation and perfect cooling.

Bistability model for automatic fitting The recorded skewed resonances are fitted with the following model in order to extract the resonance drag $\delta\omega$ accurately. The dropped power can be expressed using the usual model of a Lorentzian cavity response as:

$$P_d = \kappa_0 |a|^2 = \frac{\kappa_0 \kappa_{\text{ex}}}{\Delta\omega_{\text{hot}}^2 + \left(\frac{\kappa}{2}\right)^2} \quad (\text{S1})$$

$$= \frac{\kappa_0 \kappa_{\text{ex}}}{(\Delta\omega - \delta\omega)^2 + \left(\frac{\kappa}{2}\right)^2} = \frac{\kappa_0 \kappa_{\text{ex}}}{(\Delta\omega - \alpha P_d)^2 + \left(\frac{\kappa}{2}\right)^2} \quad (\text{S2})$$

here $|a|^2$ is the number of photons of in the resonator mode, κ_0 and κ_{ex} are the internal loss and coupling rate which form together the resonance decay rate $\kappa = \kappa_{\text{ex}} + \kappa_0$. The hot resonance detuning $\Delta\omega_{\text{hot}}$ can be expressed using the resonance drag $\delta\omega$ as $\Delta\omega_{\text{hot}} = \omega_{0,\text{hot}} - \omega_p = \Delta\omega_{\text{cold}} - \delta\omega$. The resonance drag is a function of the dropped power P_d with the coefficient $\alpha = \beta(\omega) R_{\text{th}} \zeta$ uniting the previously introduced coefficients. The resulting equation is cubic in the dropped power and can be written as:

$$0 = -\kappa_0 \kappa_{\text{ex}} + \left(\Delta\omega^2 + \left(\frac{\kappa}{2} \right)^2 \right) P_d - 2\Delta\omega \alpha P_d^2 + \alpha^2 P_d^3 \quad (\text{S3})$$

For a given κ_0 and κ_{ex} , this cubic equation can be solved using the Cardan roots in order to fit the measured transmission. With the fitted value for α the total resonance shift is obtained as $\delta\omega = \alpha P_d$.

Resonance frequency shift contributions The resonance frequency shift and the resulting tilted resonance shape upon laser scanning are in principle due to heating effects and the nonlinear phase shift. For our above analysis it is important to rule out a significant contribution of the nonlinear effects. The total resonance drag including thermal and nonlinear contributions can be expressed as:

$$\delta\omega = \alpha P_d + \frac{\omega_0 n_2}{n_0 A_{\text{eff}}} P_d \quad (\text{S4})$$

Figure 3b) shows the typical values for dropped powers and resonance drag obtained in the experiment. A resonance drag of 30 MHz is measured for a dropped power of 0.2 mW. Using the literature value for $n_2 = 2.5 \times 10^{-19} \text{ m}^2 \text{ W}^{-1}$ and the waveguide dimensions we estimate a nonlinear contribution of ≈ 4 kHz for the given experiment conditions. Thus the nonlinear contribution can be considered negligible.

3. AFM MEASUREMENTS OF SIDEWALL ROUGHNESS

In order to measure the waveguide's sidewall roughness the AFM tip needs to be brought into proximity of the sidewall surface. Providing access for the AFM tip to the waveguide's sidewall can be challenging, and different techniques ranging from sample cleaving, etched fins [3] and 3D AFM tools using special tips have been developed [4].

Here, we etch straight recesses using an amorphous silicon hardmask and electron beam lithography, as applied in the photonic Damascene process, into a $2 \mu\text{m}$ thick wet thermal SiO_2 layer. After smoothing the SiO_2 surface with the reflow process, the recess structures are sliced by etching deep trenches running across them. After removing the surrounding wafer substrate, the straight recess sample provides access to the AFM tip, when entering it upright into the AFM tool, as shown in Figure S2b). Standard Si tips with 5 nm radius are used to scan in peak-force mode along the sidewall and careful navigation is necessary in order to move the tip onto the surface of the reflowed recess. An example measurement is shown in Figure S2c), where the reflowed recess sidewall is much smoother compared to the etched SiO_2 surface that was etched for slicing the recess. At the transition between both sections the signal diverges due to the ill defined tip movement at the sharp edge. On the measured length scale of $4 \mu\text{m}$ the recess sidewall roughness is dominated by the central kink of approximately 10 nm amplitude. We attribute this kink to an aliasing artifact during layout fracturing for electron beam lithography which is based on a 10 nm grid in the present case. Using careful fracturing and a multipass writing strategy such defects can be eliminated [5].

In order to obtain quantitative values for the roughness on all waveguide surfaces, we additionally perform AFM measurements on the Si_3N_4 surfaces of a sample wafer after planarization. For further data analysis the topography data acquired on recess sidewalls and on the Si_3N_4 top surfaces is cropped and levelled, removing irrelevant measurement data and subtracting a linear background. Next, the 1-D auto-correlation

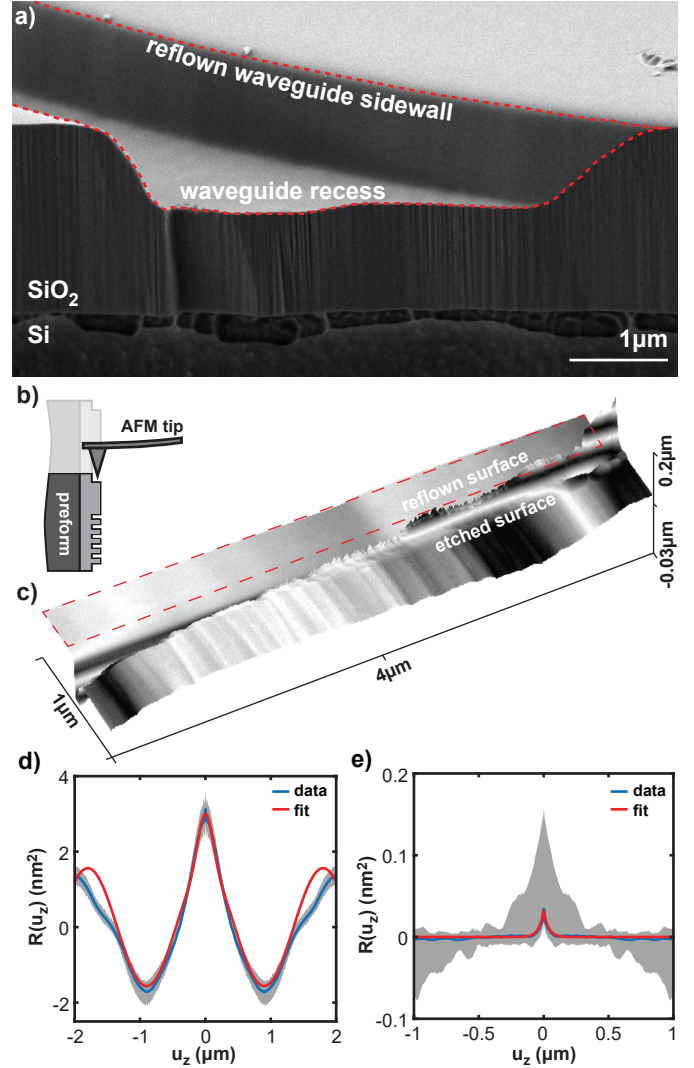


Fig. S2. AFM measurement of sidewall roughness. a) Ring waveguide recess in a SiO_2 preform after the reflow step. Smoothing of the dry etch induced sidewall roughness results in hardly perceived surface roughness and rounding of the sharp edges. b) Illustration of the AFM tip approaching the sidewall of a cut-open waveguide recess when entering the sample into the AFM tool. c) Surface topography acquired using AFM when scanning over a reflowed waveguide surface (red dashed area). Diverging signals are observed at the transition from the dry etched SiO_2 bulk to the reflowed surface. d), e) 1-D autocorrelation functions $R(u_z)$ calculated based on the traces acquired on the reflowed waveguide recess sidewall (red dashed area in c) and the Si_3N_4 waveguide top surface after CMP, respectively. The minimum and maximum limits are indicated in grey, while the mean value in blue is used for fitting. While the top surface roughness has a low amplitude and short correlation length, the sidewall autocorrelation is dominated by the periodic variations due to the kink in the sidewall profile visible in c).

functions $R(u_z) = \sum f(z)f(z + u_z)$ are calculated for each trace in the AFM scanning direction which was chosen to coincide with the propagation direction of the optical mode in the waveguide. Figure S2d) shows the resulting mean, as well

sample	Cr	Mn	Fe	Co	Ni	Cu	Zn
1 μm LPCVD Si_3N_4	< 0.1	< 0.05	0.08	< 0.05	< 0.05	0.12	0.29
3 μm LTO	0.17	0.13	2.0	< 0.05	0.11	0.24	< 0.5
4 μm wetOx	0.13	< 0.05	0.7	< 0.05	0.12	0.17	< 0.5

Table S2. Summary of the transition metal impurity concentration found in as-deposited thin films forming the core, lower and upper cladding of the Si_3N_4 waveguides. All concentrations are given in ppm wt.

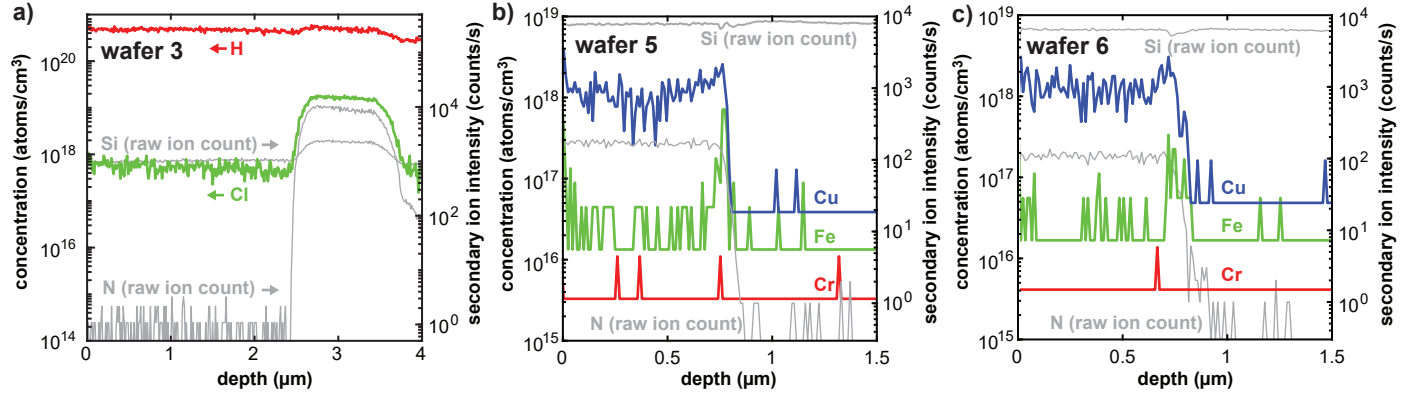


Fig. S3. Further SIMS characterization data. a) Measured profile of hydrogen and chlorine within a sample of wafer 3. Chlorine is mostly present in the silicon nitride core as the LPCVD deposition process uses dichloro silane (SiCl_2H_2) as precursor. The concentration of hydrogen is almost constant across the sample. b,c) Transition metal impurity profiles acquired for cladding-less samples from wafer 5 and 6. Again significant copper impurity concentrations are found and in addition low quantities of iron at the interface between core and cladding. All values are quantified based on Si_3N_4 standards.

as the minimum and maximum values of $R(u_z)$ obtained for the $0.37 \times 4 \mu\text{m}^2$ red dashed area on the recess sidewall in S2c). The mean auto-correlation function can be well fitted using a model composed of either an exponential or Gaussian auto-correlation function, $R_{\text{exp}}(u_z) = \sigma_{\text{exp}}^2 \exp(-|u_z|/d_{\text{exp}})$ or $R_G(u_z) = \sigma_G^2 \exp(-(u_z/d_G)^2)$, superimposed on a periodic correlation function $R_p(u_z) = \sigma_p^2 \cos(2\pi u_z/d_p)$, where $\sigma_{G,\text{exp},p}$ are the rms deviations and $d_{G,\text{exp},p}$ the correlation lengths. We extract values of $\sigma_p = 1.2 \text{ nm}$ and $d_p = 1.8 \mu\text{m}$, $\sigma_{\text{exp}} = 1.35 \text{ nm}$ and $d_{\text{exp}} = 120 \text{ nm}$ or $\sigma_G = 1.2 \text{ nm}$ and $d_G = 155 \text{ nm}$. Similarly, the mean autocorrelation function for the measured waveguide top surface roughness after CMP is well fitted by a pure exponential or Gaussian model as shown in Figure S2e). We extract values of $\sigma_{\text{exp}} = 0.18 \text{ nm}$ and $d_{\text{exp}} = 36 \text{ nm}$ for the correlation amplitude and rms deviation with the exponential autocorrelation function, and respectively $\sigma_G = 0.18 \text{ nm}$ and $d_G = 50 \text{ nm}$ with the Gaussian autocorrelation function. Neglecting the periodic roughness contribution, which causes Bragg type reflections for certain resonance frequencies only, the measured correlation length of the recess sidewall roughness is similar to previous works on Si and InP waveguides [6–8]. On the contrary the estimated rms deviation is lower than previously reported values for Si_3N_4 waveguides [3].

4. MATERIAL CHARACTERIZATION

The glow discharge mass spectroscopy (GDMS) measurements discussed in the main section were performed at Evans Analytical Group. For this purpose the wafer substrates with the respective thin films were cleaved into coupons of at least $15 \times 15 \text{ mm}^2$. The stated concentrations are derived from the stabilized signal

levels after some sputtering time. Calibration standards are used to convert the signal levels into concentration values. Table S2 summarized the results found in the as-deposited thin films.

Figure S3 provides additional measurement data for the samples of this study. The measurements were acquired at Evans Analytical Group using O_2^+ bound SIMS for profiling of transition metals and Cs^+ bound SIMS for the profiling of chlorine and hydrogen. The measurements were performed on an at least $10 \times 10 \text{ m}^2$ large area on a regular chip with working microresonator devices. The matrix signal (N and Si) is shown as raw ion count to enable distinction of the material layers. The impurity values are calibrated based on a silicon nitride standard such that values obtained within the oxide layer can be imprecise.

Hydrogen is found in concentrations of $\sim 5 \times 10^{20} \text{ atoms/cm}^3$ ($\approx 5000 \text{ ppm wt}$) almost constant across the device stack. Chlorine is detected within the Si_3N_4 core which can be easily explained by the chlorine containing LPCVD precursor gases. Copper is detected again in both samples at concentrations of $\sim 10^{18} \text{ atoms/cm}^3$ ($\approx 10 \text{ ppm wt}$). Interestingly, also iron peaks are detected in proximity of the interface between core and cladding.

REFERENCES

1. P. Marin-Palomo, J. N. Kemal, M. Karpov, A. Kordts, J. Pfeifle, M. H. Pfeiffer, P. Trocha, S. Wolf, V. Brasch, M. H. Anderson, R. Rosenberger, K. Vijayan, W. Freude, T. J. Kippenberg, and C. Koos, “Microresonator-based solitons for massively parallel coherent optical communications,” *Nature* **546**, 274–279 (2017).
2. X. Xue, Y. Xuan, C. Wang, P.-H. Wang, Y. Liu, B. Niu, D. E.

- Leaird, M. Qi, and A. M. Weiner, "Thermal tuning of Kerr frequency combs in silicon nitride microring resonators," *Opt. Express* **24**, 687–698 (2016).
3. S. P. Roberts, X. Ji, J. Cardenas, A. Bryant, and M. Lipson, "Sidewall Roughness in Si₃N₄ Waveguides Directly Measured by Atomic Force Microscopy," *Cleo:2017* pp. 5–6 (2017).
 4. J. H. Jang, W. Zhao, J. W. Bae, D. Selvanathan, S. L. Rommel, I. Adesida, A. Lepore, M. Kwakernaak, and J. H. Abeles, "Direct measurement of nanoscale sidewall roughness of optical waveguides using an atomic force microscope," *Appl. Phys. Lett.* **83**, 4116–4118 (2003).
 5. X. Ji, F. A. S. Barbosa, S. P. Roberts, A. Dutt, J. Cardenas, Y. Okawachi, A. Bryant, A. L. Gaeta, and M. Lipson, "Ultra-low-loss on-chip resonators with sub-milliwatt parametric oscillation threshold," *Optica*, **4**, 619–623 (2017).
 6. M. Borselli, K. Srinivasan, P. E. Barclay, and O. Painter, "Rayleigh scattering, mode coupling, and optical loss in silicon microdisks," *Appl. Phys. Lett.* **85**, 3693–3695 (2004).
 7. J. H. Jang, W. Zhao, J. W. Bae, D. Selvanathan, S. L. Rommel, I. Adesida, A. Lepore, M. Kwakernaak, and J. H. Abeles, "Direct measurement of nanoscale sidewall roughness of optical waveguides using an atomic force microscope," *Appl. Phys. Lett.* **83**, 4116–4118 (2003).
 8. C. G. Poulton, C. Koos, M. Fujii, S. Member, A. Pfrang, and T. Schimmel, "Radiation Modes and Roughness Loss in High Index-Contrast Waveguides," *IEEE J. Sel. Top. Quantum Electron.* **12**, 1306–1321 (2006).